PCCP

RSC Publishing

COMMUNICATION

View Article Online
View Journal | View Issue

Integrated microfluidic test-bed for energy conversion devices†

Cite this: *Phys. Chem. Chem. Phys.*, 2013, **15**, 7050

Received 27th March 2013,
Accepted 27th March 2013

DOI: 10.1039/c3cp51302e

www.rsc.org/pccp

Miguel A. Modestino,‡[abc] Camilo A. Diaz-Botia,‡[d] Sophia Haussener,[cef] Rafael Gomez-Sjoberg,[d] Joel W. Ager*[bc] and Rachel A. Segalman*[abc]

Energy conversion devices require the parallel functionality of a variety of components for efficient operation. We present a versatile microfluidic test-bed for facile testing of integrated catalysis and mass transport components for energy conversion *via* water electrolysis. This system can be readily extended to solar-fuels generators and fuel-cell devices.

Considerable innovation will be required in energy conversion technologies in order to achieve a sufficient amount of sustainable energy in the future.[1] One challenge to increasing the portion of power from renewable sources (*e.g.* solar and wind) in the existing electrical grid is their dilute, intermittent, and stochastic nature. Significant amounts of energy storage need to be realized to mitigate these problems and allow for larger amounts of solar energy to be incorporated in the current energy landscape.[2] Electrochemical devices such as redox flow batteries seem to be promising candidates to address this challenge and are currently being developed.[3–5] Recently, the direct electrochemical conversion of solar energy into storable fuels such as hydrogen[6] or hydrocarbons *via* the reduction of H_2O and CO_2 [7] – also considered artificial photosynthesis – has gained significant interest.[8–12] The operating principles of devices which perform electrochemical solar to fuel conversion have considerable overlap with the redox flow batteries mentioned above and with their energy utilization counterpart, the fuel cell. These include selective catalysis at the cathode and anode, minimization of cross-over losses, and management of reactant mass transport (convection, diffusion).

While there have been a number of artificial photosynthesis demonstrations which have achieved attractive solar to hydrogen conversion efficiencies,[13–17] relatively few have included all of the above principles, especially the chemical isolation of the cathode (reduction) and anode (oxidation sites). Although these examples demonstrate efficient generation of fuels from sunlight, the simultaneous separation of fuels and transport of charged intermediates necessary for the realization of practical devices is still an unresolved challenge. In the last 10 years, microfluidic fuel cells have been developed with the goal of exercising control over ion and mass transport.[18] While the goal of many of these studies is the elimination of the proton conducting membrane required in a PEM fuel cell,[19,20] some studies have targeted the optimal use of this component.[21] In this work, we apply a microfluidic design methodology to electrochemical fuel generation that can be directly adapted to solar-driven water electrolysis and can serve as a test-bed for catalyst, membrane and light-absorber components. Microfluidic electrochemical devices provide a simple route to integrate multiple components at small scales; they also provide a platform to readily tune architectures (*i.e.* channel dimensions), high degree of control over reactant and product flows, low transport limitations due to small channel dimensions and easy exchange of active materials. Here we demonstrate a microfluidic electrolyzer for water splitting in which different anode and cathode materials can be integrated and electrically accessed, transport of charged intermediates occurs through an ion conducting polymer membrane, and electrolysis products can be evolved and collected in separated streams. The system described in this work allows all the components to be incorporated, easily exchanged and tailored at scales amenable to research activities; in this way allowing for the performance of integrated devices to be readily assessed. Also, the proposed

[a] *Department of Chemical and Biomolecular Engineering, University of California, Berkeley, CA 94720, USA. E-mail: segalman@berkeley.edu*
[b] *Materials Sciences Division, Lawrence Berkeley National Laboratory, Berkeley, CA 94720, USA. E-mail: jwager@lbl.gov*
[c] *Joint Center for Artificial Photosynthesis, Lawrence Berkeley National Laboratory, Berkeley, CA 94720, USA*
[d] *Engineering Division, Lawrence Berkeley National Laboratory, Berkeley, CA 94720, USA*
[e] *Environmental Energy Technologies Division, Lawrence Berkeley National Laboratory, Berkeley, CA 94720, USA*
[f] *Institute of Mechanical Engineering, Ecole Polytechnique Fédérale de Lausanne, 1015 Lausanne, Switzerland*

† Electronic supplementary information (ESI) available: Detailed channel and electrode diagrams for microfluidic devices, calculated potential profiles across channels and video of device under operation. See DOI: 10.1039/c3cp51302e

‡ Authors contributed equally.

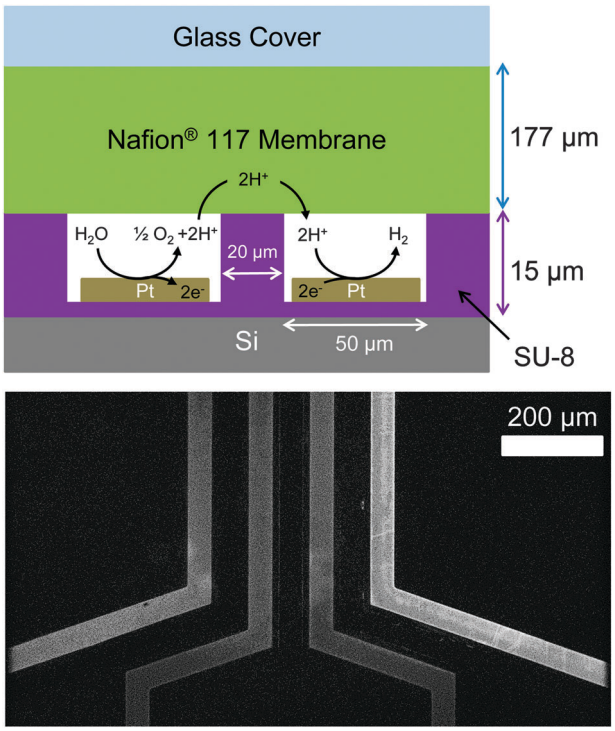

Fig. 1 Top figure presents a diagram of microfluidic electrolyzer composed of structural SU-8 channels fabricated on top of a silicon substrate and capped with a Nafion membrane for ion transport across channels. Platinum electrodes were deposited on either set of channels for water oxidation and reduction. The image in the bottom corresponds to an optical micrograph of the device with half the channels filled with a fluorescent dye aqueous solution (bright channels).

design can be easily adapted to allow direct solar irradiation and, consequently, artificial photosynthesis.

As depicted in Fig. 1, the general design developed in this work uses parallel interdigitated channels into which water oxidation and reduction electrocatalysts are deposited independently from each other. The design serves as a general framework for the fabrication of multiple microfluidic electrolyzers in which different substrates, electrodes and membrane materials can be easily incorporated and tested. To perform water electrolysis, devices need to transport charge to electrodes, reactants need to be fed to catalytic centers, products need to be extracted and ionic transport both from the electrolyte to catalytic centers and across channels needs to occur. In the proposed design, oxidation and reduction sites are separated by inert walls (fabricated with epoxy-based photoresist, SU-8) and are capped by a perfluorosulfonic acid membrane (Nafion®) that allows for proton conduction across channels. In this architecture, reactants (*i.e.* aqueous electrolyte solutions) can flow through channels, react at electrocatalyst surfaces deposited at the bottom of channels and evolve O_2 and H_2 in separated streams that are carried out of the device. Details of the fabrication and modeling approach are found in the experimental section. Although solar to H_2 conversion was not explored experimentally in this work, this functionality can be added in a straightforward manner by the fabrication of ohmically connected photocathodes and photoanodes in the reduction and oxidation channels, respectively.

In our experimental realization of the design, a series of 19 parallel channels were fabricated in each device (interdigitated anode and cathode channels), with a total active area of 8 mm^2. The anode and cathode channels are electrically accessed independently through macroscopic contacts patterned in the outside of the microfabricated chips, which allow for the electrochemical characterization of the devices. Fig. 1 shows a set of channels carrying fluorescent dyes demonstrating that independent streams can be flown through parallel channels without leakage, and Fig. S1 in the ESI† shows the detailed design of both the channels and electrodes used for the fabrication of microfluidic electrolyzers. One of the main advantages of this microfluidic design is the low ohmic resistance due to ion-transport across channels, verified by a multi-physics computational model. The device dimensions were chosen so that protons could easily diffuse through the electrolyte and the capping membrane from the oxidation side to the reduction side, and only catalyst overpotential dominated the electrochemical behavior of the system. Fig. S2 in the ESI† shows the 2-dimensional potential pattern across parallel channels for cases of high current densities (800 A m^{-2}), demonstrating the small ohmic losses in the system.

Since Nafion was selected as the capping membrane material for devices, it was convenient to carry out electrocatalytic water splitting under acidic conditions (*e.g.* sulfuric acid solutions as the feed stream). To demonstrate that the devices allow for mass transport across channels, two different pH feed streams (acidic stream pH = 1.2, near-neutral stream pH = 6.5) were flowed through parallel channel sets at a mean flow rate of 0.04 ml h^{-1} per channel, and the pH of the outlet stream was characterized. After the different electrolyte streams passed through the device, the pH of the acidic and basic sides equilibrated to pH values of 1.3 and 2.9 respectively, demonstrating mass transport across parallel channels of the device. This result correlated well with the calculated electrolyte concentration for each channel, obtained by solving the coupled mass, momentum, and species conservation equations using commercial CFD solvers for the microfluidic architecture described above (Fig. 2).

To characterize the electrochemical properties of the devices, a model integrated system with platinum electrodes in both the oxidation and reduction channels was fabricated. As previously described, a Nafion membrane was used for proton transport and a 0.5 M H_2SO_4 electrolyte was used as the feed stream. Current density and potential characteristics were obtained by sweeping potentials and measuring electrical current across the electrodes (Fig. 3). At potentials below 1.23 V (equilibrium potential for water splitting) the recorded currents are attributed to a combination of the formation of a double-layer region and a Pt-oxide region, $Pt + H_2O \rightarrow PtOH + H^+$, dominating at potentials of 0.5 to 0.6 V. Only at potentials larger 1.23 V the desired oxygen evolution reaction takes place at the anode.[22,23] Consequently, the experimental data was corrected for the double-layer resistance and compared to a simple analytical electrochemical model. The detailed 3D multi-physics model showed that the solution and membrane ohmic resistance can be neglected as it is significantly lower than the overpotential for the oxygen evolution reaction (OER) and the hydrogen

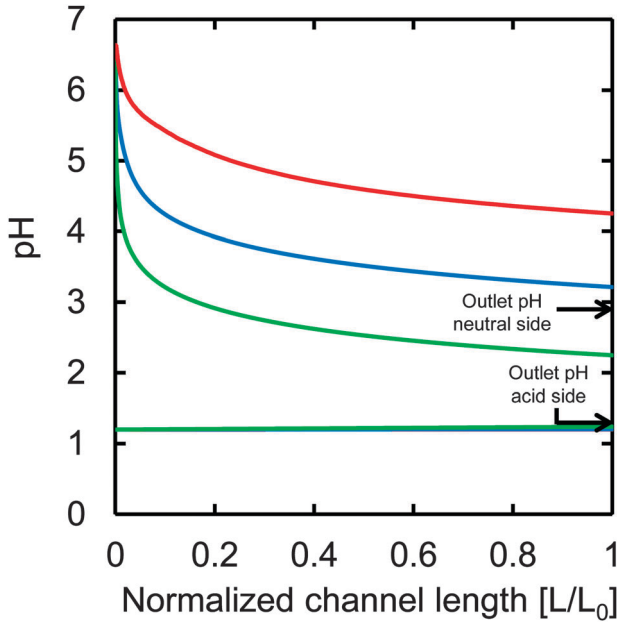

Fig. 2 Mass transport across channels as a function of channel length calculated for a series of different flow rates: 0.6 mL h^{-1} (red), 0.06 mL h^{-1} (blue), 0.006 mL h^{-1} (green). The top three lines correspond to calculated pH for the channels carrying neutral solutions while the bottom lines correspond to channels carrying acidic solutions. pH traces corresponding to the acidic channels overlap on top of each other due to the small changes in pH along the channel length. Arrows to the right of the plot indicate experimental pH values measured at the outlet of the microfluidic device. The channel length was normalized by the mean channel length (L_0 = 12.5 mm).

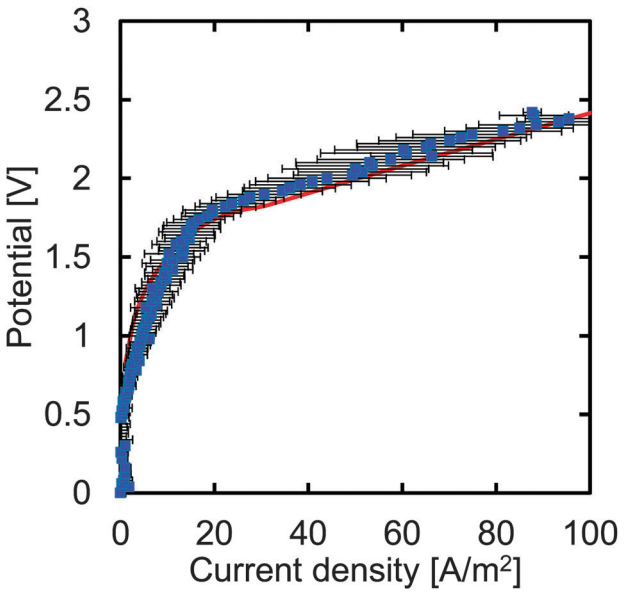

Fig. 3 Experimental (blue squares) and modeled (red line) *I–V* characteristics of microfluidic device operating with a 0.5 M sulfuric acid feed stream, and platinum catalyst for both the hydrogen and oxygen evolution reactions. Multiple traces were obtained from the devices and the error bars correspond to the standard deviation in the current measurement.

evolution reaction (HER). Additionally, the parasitic Pt-oxidation reaction at lower potentials, and resistive losses in the connectors were accounted for, leading to the following expression for the potential across channels,

$$\Phi = f(E_{0,\text{parasitic}} + \eta_{\text{overpotential,anode,parasitic}}) + (1 - f) \times (E_0 + \eta_{\text{overpotential,anode}} + \eta_{\text{overpotential,cathode}}) + R_i$$

where f represents the fraction of Pt surface sites blocked by PtOH and is assumed to linearly decrease from 1 to 0 between 1.5 and 1.8 V, according to the change in slope of the measured data. E_0 represents the equilibrium potential for the parasitic side reaction (assumed to be 0.5 V)[22,23] and the water splitting reactions (1.23 V at the conditions considered). $\eta_{\text{overpotential}}$ are the overpotentials due to the reactions described by Tafel type expressions,

$$\eta_{\text{overpotential}} = A \log\left(\frac{i}{i_0}\right)$$

with Tafel-slope A (fitted to 0.6 V per decade for the parasitic reaction, and 0.035 V per decade for OER and HER) and exchange current density i_0 (fitted to 0.3 A m^{-2} for the parasitic reaction, and 10^{-8} A m^{-2} and 10 A m^{-2} for OER and HER).[24] R is the normalized electrode resistance, which accounts for contact resistances and non-idealities in the solid conductor and was fitted to 0.008 Ωm^2. Computed results from this model are in good agreement with experimental results as can be noted in Fig. 3. These results demonstrate that by using the described microfluidic system in conjunction with electrochemical models, direct electrochemical characterization of integrated devices can be realized and the observed performance can be explained by the combination of all the processes involved in the water splitting process. This type of analysis can enable the fast evaluation of a variety of catalyst, membranes and substrate combinations in integrated electrochemical fuel generators.

As explained above, the microfluidic system presented in this work can be used to generate electrolysis products in separated streams. Operating the model system described above at current densities up to 175 A m^{-2} resulted in steady generation of H_2 gas with a potential drops across electrodes of 2.5 V. Fig. 4 presents potential traces corresponding to current densities of 175 and 88 A m^{-2} for over 10 h of operation. The potential drops observed in this devices correlate well with the behavior observed during potential sweeps. Moreover, the traces demonstrate that the device is stable for prolonged periods of times without degradation of electrochemical properties (more than 24 h for current densities up to 175 A m^{-2} have been demonstrated). Small fluctuations in the potential traces are likely caused by the evolution of gases inside microfluidic channels resulting in a decrease of active catalyst surface area. A video of the device under operation (included in the supplemental information) demonstrates the formation of gas inside the channels and how it is rapidly flushed out of the device by the liquid streams. The results obtained in this work demonstrate that these microfluidic electrolyzers reliably generate H_2 gas and can be used to assess the performance and stability of integrated systems with interchangeable components (*i.e.* catalysts and membranes) and can be readily modified into a solar-driven electrochemical energy conversion device.

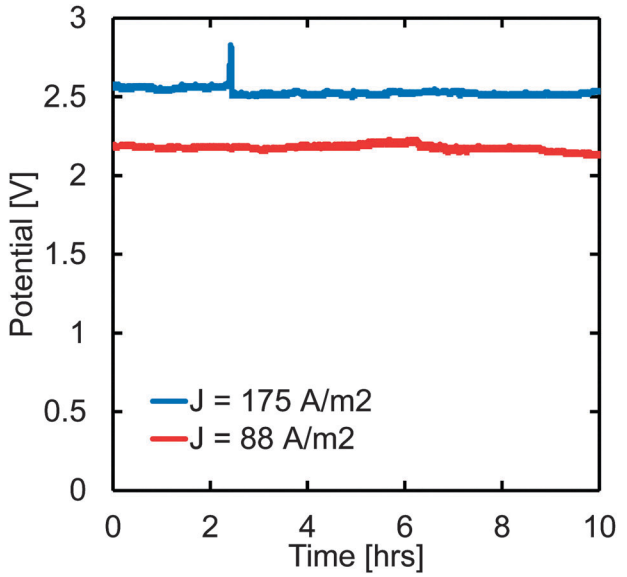

Fig. 4 Potential traces at different current densities demonstrate that the device is electrochemically stable for more than 10 hours and only small fluctuations in potential are observed as gases evolve inside the channels.

Conclusions

This work demonstrates that microfluidic electrolyzers can be fabricated and used to assess the performance of integrated devices involving catalytic and ion transport components. The microfluidic platform described here allows for the readily exchange of catalytic components and ion conducting membranes. The small scale of the devices facilitates the evaluation of new materials under development without the need for scale-up. The use of multiphysics models in combination with experimental results from operating devices, can allow for the characterization and optimization of fully integrated systems. All these attributes make this microfluidic platform a suitable test-bed for integrated electrolyzers. The system described in this work can be easily extended to a photoelectrolyzer by the incorporation of a photovoltaic component as the substrate of devices; this will further enhance its potential for aiding in the development of novel efficient components for solar-fuel generators.

Experimental section

Microfabrication

The microfluidic device was fabricated using photolithography and thin film deposition techniques. A 100 nm film of platinum was sputtered on a silicon wafer (University wafers, South Boston, MA) that had SU8 as insulator. Patterning platinum was done using a lift-off technique with SPR-220-7 positive photoresist. After the electrodes had been created on the wafer, a layer of 15 um of SU8-2025 photoresist containing the channels of the device was patterned by photolithography. Afterwards, the fluidic connections were automatically drilled using a laser mill. Once the device had been diced out of the wafer and properly cleaned, it was capped with a hydrated Nafion membrane and a glass cover slip; this assembly was then clamped in a custom made holder, with a laser-cut silicone gasket on the fluidic connection side, and a quartz window against the glass cover. Solutions were injected into the chip from custom vials that were pressurized with nitrogen provided by a custom pressure control panel.

Electrochemical characterization

Galvanodynamic and galvanostatic experiments were carried out using a Solartron 1287 potentiostat. For current scans, a range from 0–12.5 mA cm^{-2} was chosen with a sweeping rate of 0.02 mA cm^{-2} s as the potential across electrodes was measured. A total of 4 current sweeps were carried out for each experiment, and the average behavior was reported. In the case of galvanostatic experiments, the current in the devices was fixed to 17.5 and 8.8 mA cm^{-2} and the potential was measured as a function of time for over 10 h of operation.

Modeling

We use a previously developed and validated multi-physics model to predict the potential losses and the species crossover for a 3D case.[25] A brief summary of the model is given below.

Mass and momentum (laminar flow) conservation equations,

$$\nabla\cdot\mathbf{u} = 0 \tag{1}$$

$$\rho\mathbf{u}\cdot\nabla\mathbf{u} = -\nabla p + \mu\nabla\mathbf{u} \tag{2}$$

with density ρ, pressure p, viscosity μ, and $\mathbf{u}$ the velocity vector, are solved for the pressure and velocity fields. The steady-state governing conservation and transport equations are given by the definition of the ionic current,

$$\mathbf{i}_l = F\sum_i z_i\mathbf{N}_i \tag{3}$$

The Nernst–Planck equation for species transport and conservation,

$$\mathbf{N}_i = -z_i u_{i,e} F c_i \nabla\Phi_i - D_{i,e}\nabla c_i + \mathbf{u}c_i \tag{4}$$

$$0 = -\nabla\cdot\mathbf{N}_i + R_i \tag{5}$$

where $\mathbf{N}_i$ is the molar flux vector, R_i is the reaction source term (*i.e.* $R_i = A_0 i_R$), z_i and c_i are the valence and concentration of species i, respectively, F is Faraday's constant, and $u_{i,e}$ and $D_{i,e}$ are the effective mobility and diffusivity of species i, respectively, are – together with the electroneutrality requirement – solved for the determination of the species, current density and potential fields. The values of $u_{i,e}$ and $D_{i,e}$ are related by the Nernst–Einstein relationship for charged species (*i.e.* $u_{i,e} = D_{i,e}/RT$). The term "effective" refers to heterogeneous media such as the membrane. The reaction current density, i_R, is modeled by using Butler–Volmer expressions,

$$i_{R,\mathrm{OER/HER}} = i_{0,\mathrm{OER/HER}}\left[\left(\frac{c_{\mathrm{red}}}{c_{\mathrm{red},0}}\right)^{\gamma_{\mathrm{red}}}\exp\left(\frac{\alpha_{\mathrm{a,OER/HER}}F(\Phi_s-\Phi_l-U_0)}{RT}\right) - \left(\frac{c_{\mathrm{ox}}}{c_{\mathrm{ox},0}}\right)^{\gamma_{\mathrm{ox}}}\exp\left(\frac{\alpha_{\mathrm{c,OER/HER}}F(\Phi_s-\Phi_l-U_0)}{RT}\right)\right] \tag{6}$$

where $i_{0,\mathrm{OER}}$ and $i_{0,\mathrm{HER}}$ are the OER and HER exchange current densities, respectively, and $\alpha_{a,i}$ and $\alpha_{c,i}$ are the OER and HER

anodic and cathodic transfer coefficients, respectively, and U_0 is the equilibrium potential.

The boundary conditions are specified as concentrations and flow rates at the anode and cathode channel inlets, and the applied current density is defined at the anode and cathode channel bottom. A commercial finite-element solver, Comsol Multiphysics©, was used to solve the coupled equations with the corresponding boundary conditions.

Acknowledgements

This material is based upon work performed by the Joint Center for Artificial Photosynthesis, a DOE Energy Innovation Hub, as follows: the electrochemical and transport characterization was supported through the Office of Science of the U.S. Department of Energy under Award no. DE-SC0004993; the development of the microfluidic devices was supported by the Engineering Division at Lawrence Berkeley National Laboratory under contract number DE-AC02-05CH11231. The authors thank Jeff Beeman for help with catalyst deposition, as well as Tyler Matthews, Kenneth Lee, Karl Walczak, and Carl Koval for helpful discussions and experimental assistance.

Notes and references

1 S. Chu and A. Majumdar, *Nature*, 2012, **488**, 294–303.
2 P. Denholm and R. M. Margolis, *Energy Policy*, 2007, **35**, 4424–4433.
3 L. Joerissen, J. Garche, C. Fabjan and G. Tomazic, *J. Power Sources*, 2004, **127**, 98–104.
4 C. P. de Leon, A. Frias-Ferrer, J. Gonzalez-Garcia, D. A. Szanto and F. C. Walsh, *J. Power Sources*, 2006, **160**, 716–732.
5 A. Z. Weber, M. M. Mench, J. P. Meyers, P. N. Ross, J. T. Gostick and Q. Liu, *J. Appl. Electrochem.*, 2011, **41**, 1137–1164.
6 J. A. Turner, *Science*, 2004, **305**, 972–974.
7 S. C. Roy, O. K. Varghese, M. Paulose and C. A. Grimes, *ACS Nano*, 2010, **4**, 1259–1278.
8 G. F. Moore and G. W. Brudgiv, *Annu. Rev. Condens. Matter Phys.*, 2011, **2**, 303–327.
9 X. Chen, S. Shen, L. Guo and S. S. Mao, *Chem. Rev.*, 2010, **110**, 6503–6570.
10 F. E. Osterloh, *Chem. Mater.*, 2008, **20**, 35–54.
11 M. G. Walter, E. L. Warren, J. R. McKone, S. W. Boettcher, Q. Mi, E. A. Santori and N. S. Lewis, *Chem. Rev.*, 2011, **111**, 5815–5815.
12 A. Kudo and Y. Miseki, *Chem. Soc. Rev.*, 2009, **38**, 253–278.
13 O. Khaselev and J. A. Turner, *Science*, 1998, **280**, 425–427.
14 S. Licht, B. Wang, S. Mukerji, T. Soga, M. Umeno and H. Tributsch, *J. Phys. Chem. B*, 2000, **104**, 8920–8924.
15 S. Y. Reece, J. A. Hamel, K. Sung, T. D. Jarvi, A. J. Esswein, J. J. H. Pijpers and D. G. Nocera, *Science*, 2011, **334**, 645–648.
16 J. Brillet, J.-H. Yum, M. Cornuz, T. Hisatomi, R. Solarska, J. Augustynski, M. Graetzel and K. Sivula, *Nat. Photonics*, 2012, **6**, 824–828.
17 G. Peharz, F. Dimroth and U. Wittstadt, *Int. J. Hydrogen Energy*, 2007, **32**, 3248–3252.
18 E. Kjeang, N. Djilali and D. Sinton, *J. Power Sources*, 2009, **186**, 353–369.
19 R. Ferrigno, A. D. Stroock, T. D. Clark, M. Mayer and G. M. Whitesides, *J. Am. Chem. Soc.*, 2002, **124**, 12930–12931.
20 E. R. Choban, L. J. Markoski, A. Wieckowski and P. J. A. Kenis, *J. Power Sources*, 2004, **128**, 54–60.
21 S. M. Mitrovski, L. C. C. Elliott and R. G. Nuzzo, *Langmuir*, 2004, **20**, 6974–6976.
22 W. Sheng, H. A. Gasteiger and Y. Shao-Horn, *J. Electrochem. Soc.*, 2010, **157**, B1529–B1536.
23 F. Kodera, Y. Kuwahara, A. Nakazawa and M. Umeda, *J. Power Sources*, 2007, **172**, 698–703.
24 P. Choi, D. G. Bessarabov and R. Datta, *Solid State Ionics*, 2004, **175**, 535–539.
25 S. Haussener, C. Xiang, J. M. Spurgeon, S. Ardo, N. S. Lewis and A. Z. Weber, *Energy Environ. Sci.*, 2012, **5**, 9922–9935.

